

Article

Synthesis of Mesoporous Ru-ZnO@g-C₃N₄ Nanoparticles and Their Photocatalytic Activity for Methylene Blue Degradation

Abuzar E. A. E. Albadri ¹, Mohamed Ali Ben Aissa ², Abueliz Modwi ^{2,*} and Sayed M. Saleh ^{1,3,*}¹ Department of Chemistry, College of Science, Qassim University, Buraidah 51452, Saudi Arabia² Department of Chemistry, College of Science and Arts at Al-Rass, Qassim University, Ar-Rass 51921, Saudi Arabia³ Chemistry Branch, Department of Science and Mathematics, Faculty of Petroleum and Mining Engineering, Suez University, Suez 43721, Egypt

* Correspondence: ab.khalid@qu.edu.sa (A.M.); e.saleh@qu.edu.sa (S.M.S.)

Abstract: Cleaning contaminated water under light with a novel type of heterogeneous photocatalysts is regarded as a critical method for wastewater resolution. Thus, a unique mesoporous Ru-ZnO@g-C₃N₄ nanocomposite with an increased surface area was synthesized through the ultrasonic technique in the presence of methanol. The X-ray diffraction pattern efficiently validated the crystal structure of the Ru-ZnO hybrid and allowed it to be integrated into the g-C₃N₄ structure. TEM imaging revealed the Ru-ZnO nanocomposite as spherical particles spread uniformly throughout the g-C₃N₄ nanosheet. X-ray photoelectron spectroscopy (XPS) was applied to determine the bonding properties of the samples. Under visible illumination, the synthesized nanocomposites of Ru-ZnO@g-C₃N₄ were evaluated as a new effective photocatalyst for degrading organic pigments in aquatic conditions.

Keywords: Ru-ZnO@g-C₃N₄; nanocomposite; ultrasonic power; RB dye destruction



Citation: Albadri, A.E.A.E.; Aissa, M.A.B.; Modwi, A.; Saleh, S.M. Synthesis of Mesoporous Ru-ZnO@g-C₃N₄ Nanoparticles and Their Photocatalytic Activity for Methylene Blue Degradation. *Water* **2023**, *15*, 481. <https://doi.org/10.3390/w15030481>

Academic Editor: Chengyun Zhou

Received: 30 December 2022

Revised: 13 January 2023

Accepted: 16 January 2023

Published: 25 January 2023



Copyright: © 2023 by the authors. Licensee MDPI, Basel, Switzerland. This article is an open access article distributed under the terms and conditions of the Creative Commons Attribution (CC BY) license (<https://creativecommons.org/licenses/by/4.0/>).

1. Introduction

Much research interest and attempts have recently been directed into metal-free visible-light active photocatalysts for organic pollutant degradation, owing to the growing need for environmental stewardship [1]. Numerous photocatalysts, including ZnO [2], TiO₂ [3], SnO₂ [4], Co₂O₄ [5], MoS₂ [6], Cu-doped ZnO [7], Ru-doped ZnO [8] and g-C₃N₄, have been explored. Amongst these, g-C₃N₄ has emerged as a promising candidate for the photocatalytic degradation of dyes due to its well-suited band gap of around 2.7 eV, enabling enhanced charge-carrier excitation via effective solar absorption. Graphitic carbon nitride (g-C₃N₄) has attracted considerable attention due to its excellent chemical stability, attractive electronic band gap, and optical properties as a metal-free, visible-light-driven semiconductor photocatalyst for solar energy conversion and environmental remediation [9–11]. Conversely, bulk g-C₃N₄ has a limited surface area and a high rate of photogenerated electrons and hole recombination, leading to low photocatalytic activity [12–14]. Extensive initiatives have been devoted to improving the photocatalytic properties of g-C₃N₄, comprising doping with heteroatoms, combining with other semiconductors, and manipulating the morphology [15–17]. Nonetheless, the facile production of extremely effective g-C₃N₄ continues to be a substantial obstacle [18,19].

Through its stable chemical composition and ineffective biodegradation, methylene blue (MB) has a relatively poor degradation efficiency under natural settings, which might be detrimental to the microflora balance in the environment and in people [20,21]. The leftover MB causes lifelong eye damage, nausea, vomiting, headache, stomach cramps, vertigo, and stomach upset [22,23]. As a result, there is a growing need to develop new solutions for its removal from water/soil resources [24–26]. Photocatalysis, a simple process and environmentally friendly technique, may decompose organic contaminants in

wastewater into water, carbon dioxide, or other tiny molecules, and decrease or oxidize inorganic pollutants into innocuous compounds [27,28]. Due to the instability of deactivated photocatalysts, the catalyst is susceptible to self-etching in photocatalysis. It has been extensively studied for the development of heterojunction structures, doping, defect synthesis to enhance photocatalytic performance, and the restoration of effective catalytic activities by oxidative reduction in deactivated photocatalysts for reprocessing.

The present study establishes a strategy for fabricating ternary Ru-ZnO@g-C₃N₄ heterostructure hybrids. In the presence of methanol, a simple in situ ultrasonic method is used to attach the Ru-ZnO photocomposite to g-C₃N₄ nanosheets. Fabricated Ru-ZnO photocomposite was utilized between the g-C₃N₄ layers in this construction, providing a new photocatalyst that enables rapid electron and hole transport. Notably, the heterostructures as proposed create a porous surface that may reduce photogenerated electron and hole recombination and act as adsorbents for dye pollutant molecules on the hybrid surface. The hybrids displayed superior photocatalytic efficiency when exposed to ultraviolet light, with incredible cyclin stability.

2. Materials and Methods

2.1. Chemicals and Materials

Zinc nitrate hexahydrate (Zn(NO₃)₂·6H₂O; ≥99.0%), ruthenium(III) chloride (RuCl₃; ≥98.0%), carbonyl diamide (CH₄N₂O, ≥99.0%), methylene blue (MB, ≥82%), sodium hydroxide (NaOH, ≥99%), sodium chloride (NaCl, ≥99%), and hydrochloric acid (HCl, 37%), purchased from Merck Company, were used without further purification.

2.2. Fabrication

We followed a well-established process to synthesize the pure g-C₃N₄ described in our previous article [16]. Carbonyl diamide (4.5 g) was placed in a crucible with an aluminum foil lid and then calcined for 120 min at 450 °C at a rate of 10 °C/min in ambient pressure air in a muffle furnace. The yellow powders were received after a period of steady cooling. To fabricate Ru-ZnO nanostructures, 0.03 moles of Zn(NO₃)₂·2H₂O solution and 0.64 g of RuCl₃ were warmed and agitated at 250 °C for 4 h with 100 mL of pectinase sugar saturation solution in a 1000 mL beaker. Following this, a brown-white foam was obtained and permitted to cool for 24 h at room temperature. Ru-ZnO nonmaterial was received by drying the brown-white powder and calcining it at 120 °C for 120 min. Ru-ZnO@g-C₃N₄ nanoparticles were produced utilizing a straightforward stage ultra-sonication method. A total of 920 mg of g-C₃N₄ was weighed and sonicated for 15 min in 150 mL of methanol. A total of 400 mg of Ru-ZnO nanoparticles were added to the methanolic mixture, followed by 15 min of sonication. The recovered yellowish suspension was sonicated for a further 45 min and drained at 85 °C for a day. Finally, the resulting nanomaterials were annealed at 180 °C.

2.3. Nanomaterials Characterization

Using a Bruker D8 Advance X-ray diffractometer (Bruker AXS, Karlsruhe, Germany) with Cu-Kα1 radiation ($\lambda = 0.15406$ nm) and a scan rate of 0.02/per second, the crystal structure of the samples was examined. The accelerating voltage was 40 kV, while 20 mA was the extracting current. An S-3400 N (Japan) field emission scanning electron microscope was employed, and scanning electron microscopy (SEM) pictures were received. A Nicolet 5700 FT-IR spectrophotometer was used to record the as-prepared samples' 400–4000 cm⁻¹ FT-IR spectra. Al Kα (1486.68 eV) X-ray sources were utilized for X-ray photoelectron spectroscopy (XPS) to determine the bonding properties of the samples (VG ESCALAB 220i-XL, West Sussex, UK). The TEM images were taken using a Tecnai G20 transmission electron microscope and a 200 kV accelerating voltage (Hillsboro, OR, USA). The BET surface area and pore size distribution of generated samples were evaluated by adsorbing N₂ at 77 K using ASAP 2020HD 88 instruments. The absorbance was determined using a UV-Vis spectrophotometer in diffuse reflection mode with BaSO₄ as the standard (UV-2550, Hamamatsu, Shizuoka, Japan).

2.4. Batch Experiments

All of the experiment series were applied to attain the optimal conditions of the degradation process of the methylene blue (MB) dye based on RuZnO@g-C₃N₄ nanomaterial nanocatalysts. The degradation of the MB dye was investigated under 360 nm UV radiation. The effect of significant factors, including the initial concentration of MB, photocatalyst dose, and pH of the studied medium, was investigated accordingly. This work conducted all experiments under optimal conditions using 100 mL MB solution of 30 ppm in a 100 mL volumetric flask. The pH experiments were performed after adjusting the pH of the solutions using 0.1M HCl and 0.1M NaOH. The investigated colloidal solutions of the mixed MB dye and RuZnO@g-C₃N₄ nanomaterials were prepared using a magnetic stirrer under 4400 rpm for 10 min. The absorbance spectra of the MB dye solutions were recorded utilizing an Evolution 200 series Thermo Fisher UV-Vis spectrophotometer.

3. Result and Discussion

3.1. Ru-ZnO@g-C₃N₄ Nanoparticles Characterization

The structural phase of the fabricated pure g-C₃N₄, Ru-ZnO, and Ru-ZnO@g-C₃N₄ photocatalysts was determined using X-ray diffraction (XRD) techniques, as illustrated in Figure 1. The two peaks of g-C₃N₄ at 12.64 °C and 27.22 °C indicated that planes (100) and (002) corresponded to the distance between the interlayer architectural package and the separation of connected aromatic systems correspondingly. The peaks of the Ru-ZnO nanocomposite observed at $2\theta = 31.55, 34.37, 36.17, 47.40, 56.53, 62.72, 66.30, 68.8,$ and 69.03° could be attributed to the (100), (002), (101), (102), (110), (103), (200), (112), and (201) planes of the wurtzite hexagonal ZnO configuration, according to JCPDS card no. 36-1451 [29]. Additionally, new peaks corresponding to $2\theta = 27.9, 34.92,$ and 54.35° were discovered, outlining the RuO₂ rutile phase's (110), (101), and (211) planes in accord with JCPDS card no. 88-0322 [30].

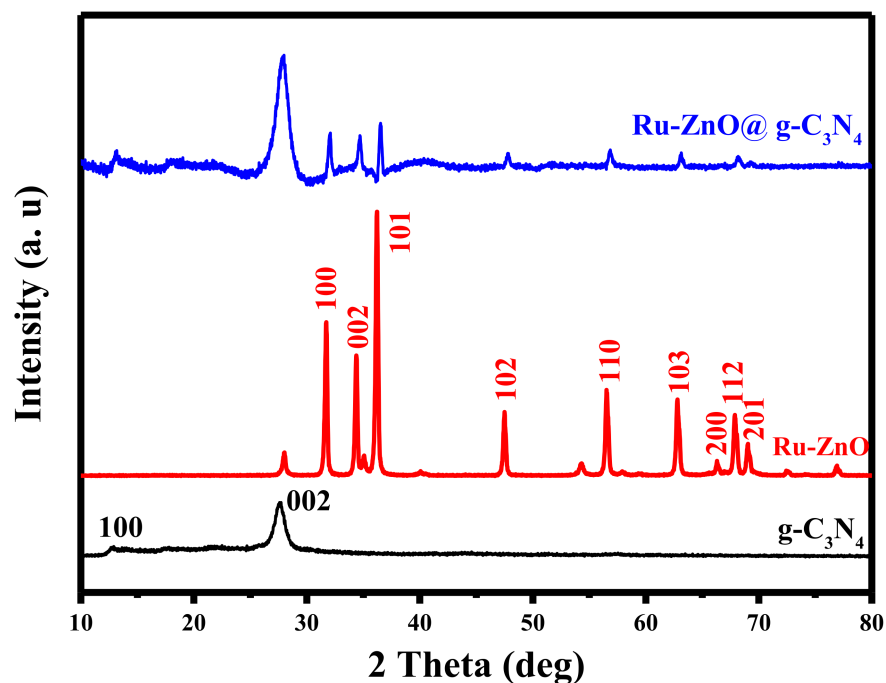


Figure 1. XRD pattern of g-C₃N₄, Ru-ZnO, and Ru-ZnO@g-C₃N₄.

The XRD pattern reveals unequivocally that the composite consists of g-C₃N₄ and Ru-ZnO diffraction peaks. A thorough inspection of the composite XRD peaks reveals a slight peak shift toward the higher angle side in the (002) plane of g-C₃N₄ but no peak shift in Ru-ZnO. This study indicated that Ru-ZnO nanoparticles were deposited on g-C₃N₄ in the nanocomposite, thereby decreasing the d-space of conjugated aromatic systems and

the crystal size. The stability of the synthesized catalyst after the degradation process was examined by XRD and there is no change between the XRD pattern before and after the degradation processes.

The morphology and the elemental distribution of pure $g\text{-C}_3\text{N}_4$, Ru-ZnO, and Ru-ZnO@ $g\text{-C}_3\text{N}_4$ photocatalysts were further revealed by field emission scanning electron microscopy (FE-SEM) coupled with energy dispersive X-ray spectroscopy (EDX). As shown in Figure 2a, the pure $g\text{-C}_3\text{N}_4$ FESEM image exhibits surface-sheet layers. The FESEM image of Ru-ZnO (Figure 2c) indicated that the morphology is a spherical shape with various particle sizes. Figure 2e suggests that the Ru-ZnO is uniformly distributed over the nanosheet structure of $g\text{-C}_3\text{N}_4$, as shown in the FE-SEM image of Ru-ZnO@ $g\text{-C}_3\text{N}_4$. The EDX spectrum of the obtained photocatalysts (Figure 2f) demonstrates typical characteristic peaks of Ru, Zn, O, C, and N, confirming the prepared photocatalysts' purity.

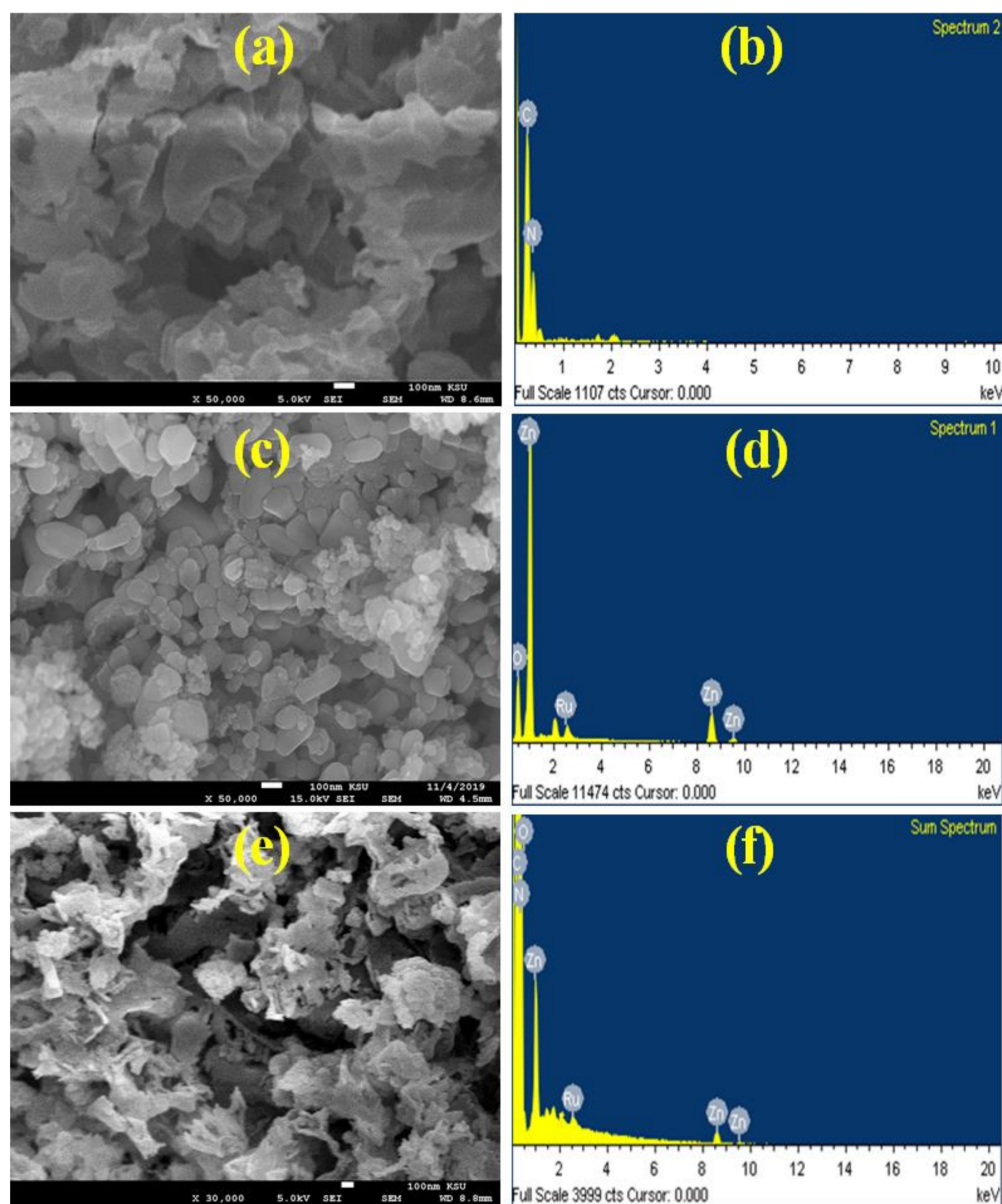


Figure 2. SEM images and EDX for the elemental composition of $g\text{-C}_3\text{N}_4$ (a,b), Ru-ZnO (c,d), and Ru-ZnO@ $g\text{-C}_3\text{N}_4$ (e,f).

FTIR spectra of pure $g\text{-C}_3\text{N}_4$, Ru-ZnO, and Ru-ZnO@ $g\text{-C}_3\text{N}_4$ photocatalysts are shown in Figure 3. For the FTIR spectra of $g\text{-C}_3\text{N}_4$ and Ru-ZnO@ $g\text{-C}_3\text{N}_4$, the typical band at

892 cm^{-1} is assigned to the triazine ring mode of heptazine. The multiple bands at 1256, 1329, and 1426 cm^{-1} represent the aromatic C–N stretching vibration, although the bands at 1579 and 1638 cm^{-1} correspond to C \equiv N stretching [31]. Moreover, the absorption band in the range of 3000–3400 cm^{-1} is ascribed to the stretching mode of the terminal amino group. Additionally, the band at 433 cm^{-1} in the FTIR spectra of Ru-ZnO and Ru-ZnO@g-C₃N₄ corresponds to RuO₂–ZnO bond-stretching [32].

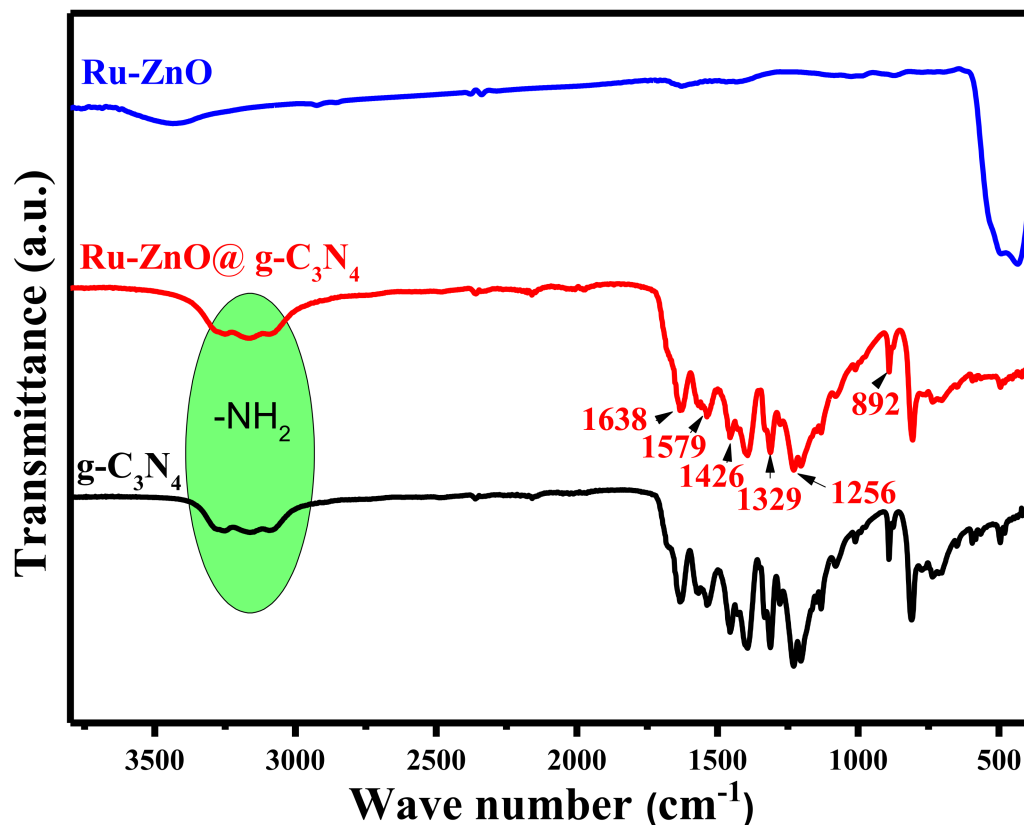


Figure 3. FTIR spectra of g-C₃N₄, Ru-ZnO, and Ru-ZnO@g-C₃N₄.

Figure 4a,c depict the nitrogen adsorption-desorption isotherms of pure g-C₃N₄ and Ru-ZnO@g-C₃N₄ nanocomposites. Due to the weak hysteresis loop creation, the Ru-ZnO@g-C₃N₄ nanostructures exhibit type IV isotherms, indicating the presence of mesoporosity during sample formation. Pure g-C₃N₄ exhibits type IV behavior, which is explained by its developing a weak hysteresis loop [33,34]. Ru-ZnO@g-C₃N₄ nanostructures have a high specific surface area of 257 m^2/g and a pore volume of 0.499 cc/g , which is more than the specific surface area of pure g-C₃N₄ (154 m^2/g and a pore volume of 0.922 cc/g). It has been demonstrated that the large specific surface area of Ru-ZnO@g-C₃N₄ nanocomposite materials enhances the photocatalytic activity for MB dye degradation; however, the surface area contributes to the nanocomposite's activity. In composite fabrication, the charge separation between the two semiconductors is also decisive.

The pore dispersion diagrams (Figure 4b,d) indicate pores with dimensions of 15 to 50 that are thin and homogeneous. The cumulative pore capacity of BJH adsorption increased from 0.37 to 0.47 $\text{cm}^3 \cdot \text{g}^{-1}$ following Ru-ZnO@g-C₃N₄ (0.87 $\text{cm}^3 \cdot \text{g}^{-1}$) hybridization. D-g-C₃N₄@Ag [35], WO₃@g-C₃N₄ [36], V₂O₅@g-C₃N₄ [37], and TiO₂@g-C₃N₄ [38] are examples of the pure g-C₃N₄ connected Ru-ZnO composite with an increased surface area. Finally, by providing a larger number of reactive sites for the photocatalytic process, the Ru-ZnO@g-C₃N₄ nanocomposite has an improved specific surface area. It is beneficial for MB dye's enhanced adsorption, enhancing its photocatalytic activity.

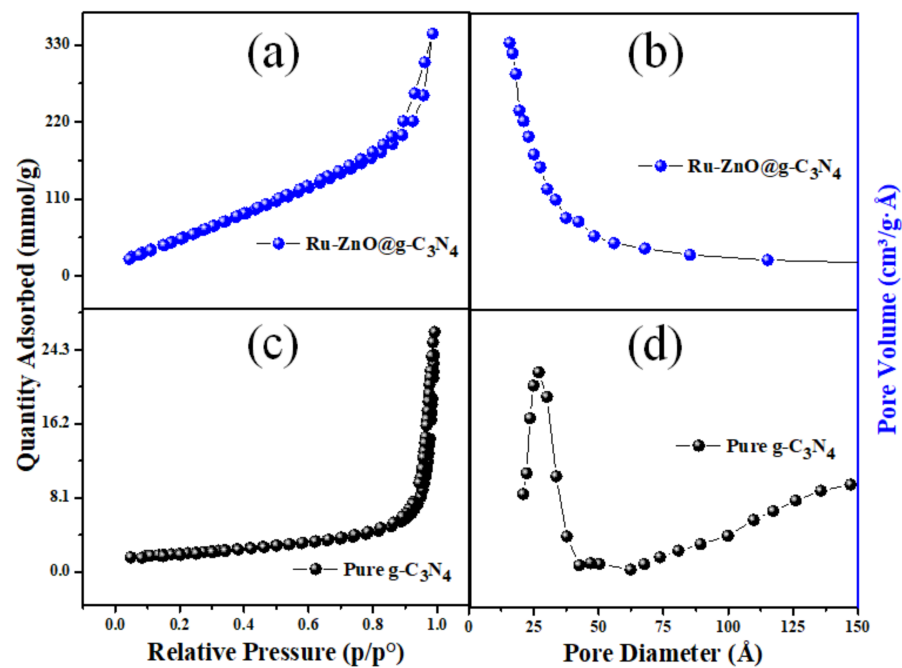


Figure 4. N_2 adsorption-desorption isotherms (a,c) pore radius distribution (b,d) of pure $g-C_3N_4$ and $Ru-ZnO@g-C_3N_4$ photocatalysts.

Figure 5a illustrates the UV-Vis spectra of $g-C_3N_4$, $Ru-ZnO$, and $Ru-ZnO@g-C_3N_4$ samples, whose absorption edges are approximately 454, 402, and 443 nm, respectively. The composite model demonstrated more photon absorption than $g-C_3N_4$ due to the composites' anticipated high crystallinity resulting from their manufacture by calcination [39]. According to the Tauc relation [40], the computed band gap energies for $g-C_3N_4$, $Ru-ZnO$, and $Ru-ZnO@g-C_3N_4$ composites are 2.77, 3.20, and 2.83 eV, respectively, as shown in Figure 5b. Confirming the XRD results, the band gap of the $Ru-ZnO$ is the typical standard value for $Ru-ZnO$. The divergence of the $g-C_3N_4$ band gap from 2.77 eV may be attributed to the creation of the $g-C_3N_4$ nanosheet, whose value is typically more significant than the bulk value of 3.20 eV reported earlier [41]. Niu et al. [42] created $g-C_3N_4$ nanomaterials with a broader band gap; they attributed this to the quantum confinement effect, which stimulates a displacement of the conduction or valence band edge of $g-C_3N_4$ [43].

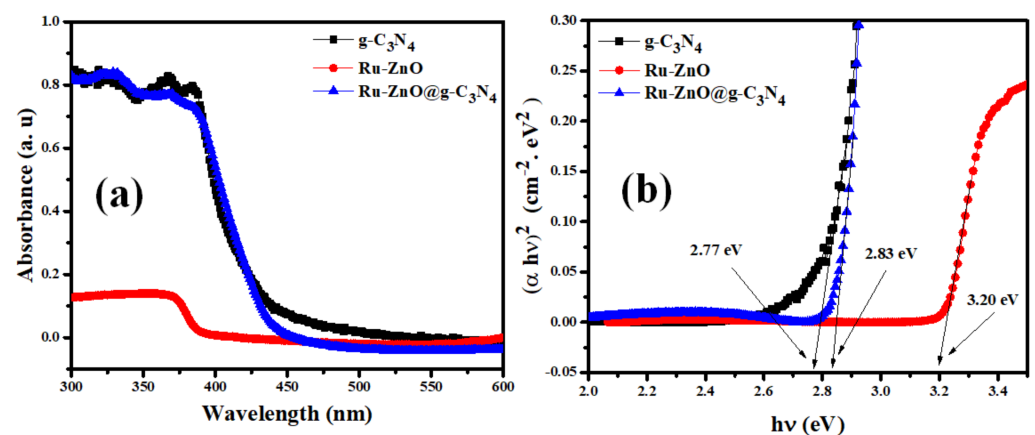


Figure 5. UV-Vis spectra (a) and bandgaps (b) of $g-C_3N_4$, $Ru-ZnO$, and $Ru-ZnO@g-C_3N_4$ nanocomposite.

By combining $Ru-ZnO$ with $g-C_3N_4$, the band gap of the $Ru-ZnO$ composite has been significantly reduced. Similar studies of heterojunctions generated by coupling $g-C_3N_4$ to semiconductors with a large bandgap to form $SrTiO_3@g-C_3N_4$ [44], $MgO@g-C_3N_4$ [45], and

ZnWO₄@g-C₃N₄ [46] with decreased band gap values have been reported. This tight interfacial interaction suggests the successful formation of heterojunctions between semiconductors. Similarly, based on the previous results, it can be concluded that Ru-ZnO has been successfully introduced into g-C₃N₄ to significantly enhance the visible light absorption capacity by photo-generated charge-carrier separation, therefore enhancing its photocatalytic properties.

The XPS technique was used to analyze the chemical oxidation states of Ru, Zn, C, N, and O in the Ru-ZnO@g-C₃N₄ photocomposite (Figure 6a). According to the 3D Ru spectrum (Figure 6b), the peak at 285.2 eV was assigned to Ru 3d_{5/2} [47]. The XPS spectra of Zn 2p core levels are shown in Figure 6c, revealing two symmetric peaks at 1047.4 and 1019.0 eV [48]. Figure 6d depicts the N1s spectra, revealing a peak at 396.4 eV, assigned to sp²-hybridized nitrogen (C-N-C) [49]. The peaks in the C 1s spectrum (Figure 6e) at 284.4 eV and 285.8 eV relate to the N-C-N coordination [49]. The XPS spectra of the O 1s core levels (Figure 6f) exhibited three peaks at 530.1, 528.3, and 526.6 eV, corresponding to lattice oxygen in ZnO, RuO₃ (Ru⁶⁺), and RuO₂ (Ru⁴⁺), respectively [50].

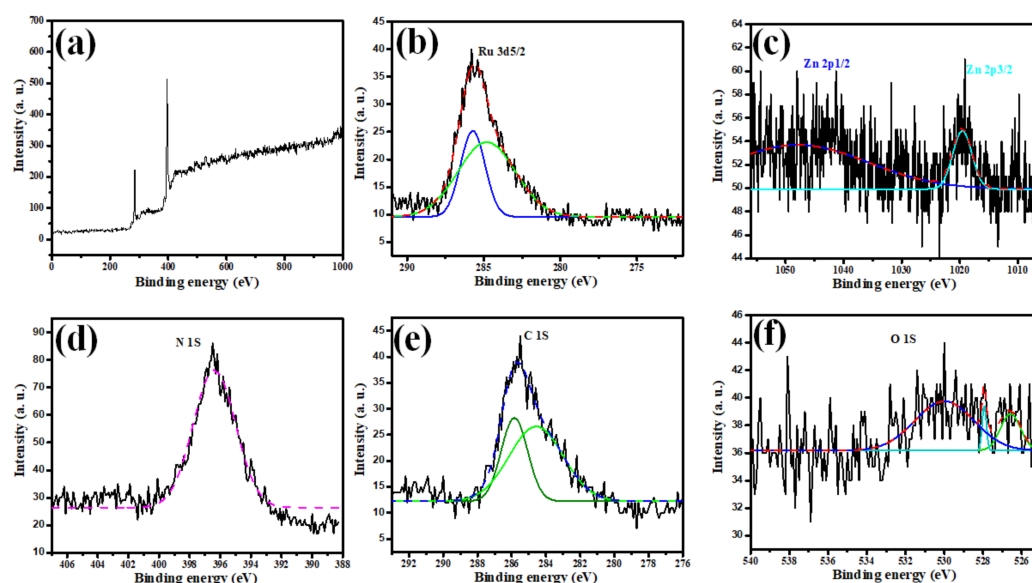


Figure 6. XPS analysis of Ru-ZnO@g-C₃N₄ photocomposite (a) full survey and individual spectra of (b) Ru 3d, (c) Zn 2p, (d) N1s, (e) C1s, and (f) O1s.

3.2. Absorption Spectra Measurements

The optical features of methylene blue are exhibited in Figure 7. The absorbance spectrum of the dye shows two prominent peaks located at 658 and 289 nm individually. When introducing Ru-ZnO@g-C₃N₄ to the dye medium, a significant quenching of the maximum absorbance peak at 664 nm is presented when exposed to UV radiation under 360 nm wavelength. The dramatic absorbance of the studied degraded dye MB based on Ru-ZnO@g-C₃N₄ nanomaterials could be referred to as their high photocatalytic activity. Additionally, the inset plot in Figure 7 presents the relation between the radiometric absorbance of the degraded dye against reaction time under UV radiation. This finding confirms that the photocatalytic degradation of MB dye is proficiently produced for 60 min only in the existence of Ru-ZnO@g-C₃N₄ nanomaterials. Additionally, the photocatalytic degradation of the MB dye was investigated utilizing Ru-ZnO@g-C₃N₄ in darkness, in the absence of UV radiation. Besides this, the measurement of MB absorbance spectra was conducted, and the results exhibit no significant alteration in the absorbance values of the dye at prominent peaks of 658 and 289 nm, respectively. MB indicates extreme photostability in darkness [51], and the process of the dye degradation does not corroborate professionally, as shown in Figure 7.

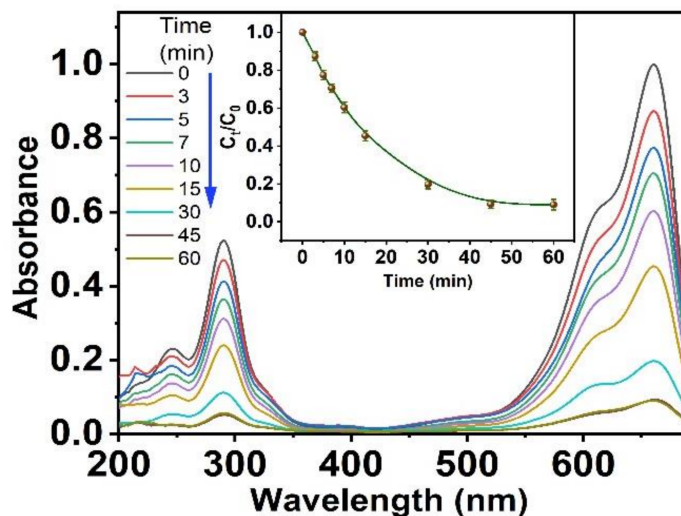


Figure 7. Absorbance spectra of methylene blue in the presence of RuZnO@g-C₃N₄ photocatalyst nanoparticles.

The resulting data displayed that the adsorption process, including the MB adsorption to the active site surface of the Ru-ZnO@g-C₃N₄ nanomaterials, is ultimately achieved after five min using a steady shaking rate in the dark, and the degradation process is considerably stopped. Therefore, the reaction mixtures were shaken under a regular stirring rate for 5 min to attain the adsorption equilibrium in all subsequent experimental series. The degradation of MB under UV brilliance is exhibited in Figure 8a, where the C₀/C_t ratio has been quenched with irradiation time; C₀ represents the initial concentration and C_t represents the degraded concentration. The degradation efficiencies were recorded as 41.5, 30.1, and 92.2% for g-C₃N₄, Ru-ZnO, and Ru-ZnO@g-C₃N₄, respectively. These results exhibit tremendous activity in RuZnO@g-C₃N₄ nanomaterials during a 60 min time interval (Figure 8a). The kinetics of the degradation were found to follow pseudo-first-order kinetics (Figure 8b) as implied by the linear relationship between ln(C₀/C_t) and radiation time, as confirmed via the high regression (R² ≈ 1). The high rate constant (k) and extremely short half-life (t_{1/2}) values in Table 1 indicate that the Ru-ZnO@g-C₃N₄ composite has enhanced photocatalytic activity. This was ascribed to dye sensitization, in which UV causes electron excitation from the dye molecule’s HOMO to LUMO, ejecting them into the ZnO conduction band and finally causing dye breakdown on the semiconductor surface.

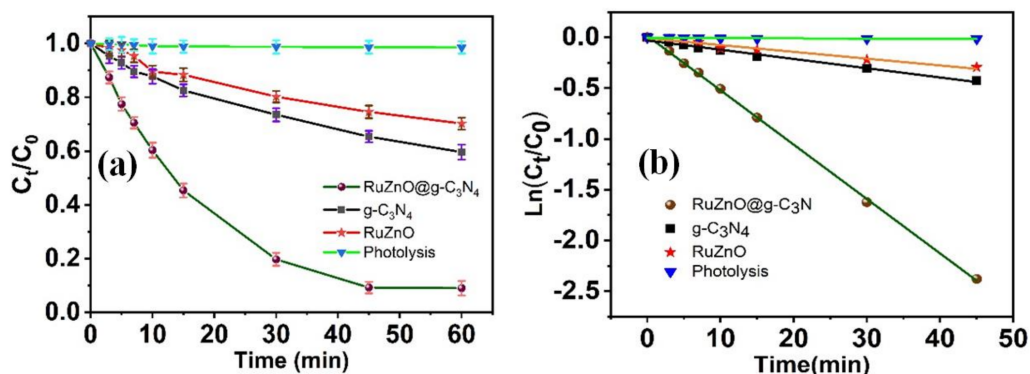


Figure 8. (a) The difference of photodegradation with time, and (b) pseudo-first-order kinetics of the methylene blue dye.

Table 1. Kinetics parameters of MB dye degradation.

Sample	K (min ⁻¹)	t _{1/2} (min)	R ²	Degradation %	Energy Gap (ev)
g-C ₃ N ₄	0.0091	76.17	0.96	19.2	2.77
ZnO	0.0066	105.02	0.98	34.6	3.2
ZnO@g-C ₃ N ₄	0.0536	12.93	0.99	91.9	2.83

3.3. Influence of MB and Photocatalyst Concentration

The photocatalytic degradation process of MB dye based on Ru-ZnO@g-C₃N₄ nanomaterials was studied in terms of the photocatalyst concentration, as shown in Figure 9. The degradation process of the MB was conducted under UV radiation and in the presence of various photocatalyst contents within the range of (25–75 mg). Remarkably, the degradation process was produced sufficiently in the existence of 75 mg of Ru-ZnO@g-C₃N₄ nanomaterials after 60 min of reaction under UV radiation. The dye degradation process is achieved where the MB molecules attain the surface of the photocatalysts. Additionally, the excellent dispersion of the small crystalline size of Ru-ZnO@g-C₃N₄ nanomaterials increases the possibility of charge permutation on the outer surface of the barrier region [52]. However, the degradation process is inversely proportional to the increment of the photocatalyst concentration when the concentration is enhanced by more than 75 mg. Thus, by increasing the photocatalyst concentration up to 75 mg, the active sites of the Ru-ZnO@g-C₃N₄ nanomaterial photocatalysts improve. This result may be referred to as the accumulation of the Ru-ZnO@g-C₃N₄ nanomaterials in the reaction medium. Therefore, the photons cannot reach the surface of the photocatalyst, and many active catalytic centers are blocked.

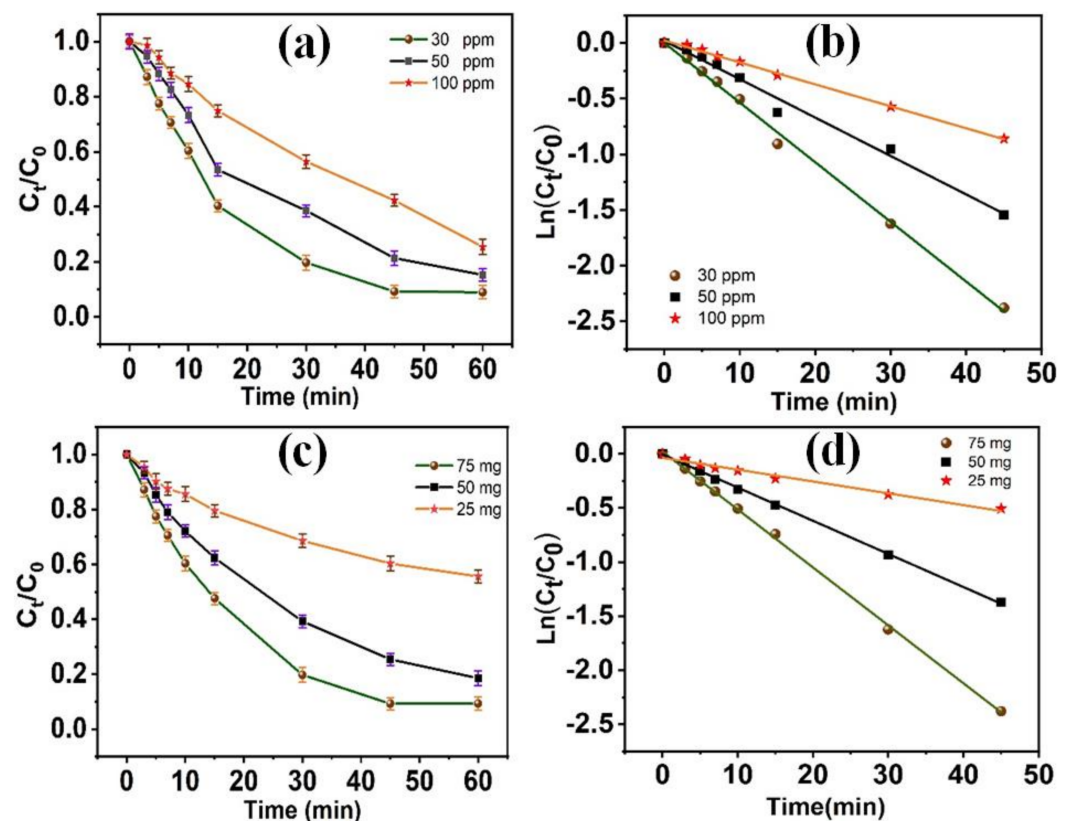


Figure 9. Photocatalytic efficiency of methylene blue dye at various concentrations (a,b) and different Ru-ZnO@g-C₃N₄ mass concentrations (c,d).

To investigate the influence of MB content in the reaction medium on the degradation process, the proper Ru-ZnO@g-C₃N₄ nanomaterial concentration was chosen to be 75 mg. The concentrations of MB ranged from 30–100 ppm for 60 min. The obtained data are exhibited in Figure 9. The results confirm that increasing the MB dye quantity influenced

the photocatalytic process depending on the Ru-ZnO@g-C₃N₄ nanomaterials. These findings can be attributed to the quenching of the number of active centers on the surface of Ru-ZnO@g-C₃N₄ nanomaterials. In that way, the generation of the hydroxyl radicals disappears, which diminishes the photocatalytic process's efficiency. Additionally, accumulating MB dye at a high concentration will reduce the photon path length that crosses the MB medium's threshold [53]. Additionally, when the MB dye concentration increases, the MB molecules absorb considerable UV radiation, influencing the photocatalytic degradation process [54,55]. Therefore, the characteristic MB concentration was designated as 30 ppm for the subsequent experiments.

3.4. pH Influence

The MB dye presents as a cationic form in the solution. The tremendous concentration of hydroxyl groups will enhance the negative surface charges on the photocatalyst surface in a basic medium. This phenomenon will change the acidic surface of the catalyst into a basic surface. Thus, the photocatalytic degradation of MB dye will be enhanced, as seen in Figure 10. Conversely, the acidic medium will repel the adsorption process. Memorably, the degradation process of the organic dye-based nano-catalysts starts with the adsorption process [56]. Thus, the activity of the photocatalysts in the degradation process mainly increases in the alkaline medium [57]. The obtained data confirm that the pH of the reaction medium is a significant parameter in the degradation process of the organic dye. Additionally, the alteration of the biting surface of the nano-catalysts affects the degradation process.

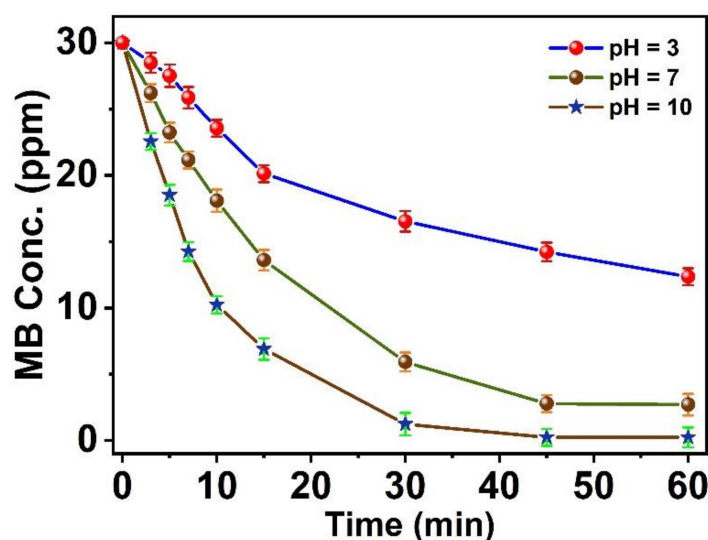


Figure 10. pH effect on the MB degradation process based on RuZnO@g-C₃N₄ nanomaterials.

3.5. Nanocatalyst Recovery

The recovery of the studied Ru-ZnO@g-C₃N₄ nanocatalysts was examined [58]. The de-coloration of the MB organic dye in the degradation process proceeded under optimum conditions and in the presence of UV radiation. The nanomaterials were easily recycled by separation and filtration with a simple washing process. The MB dye degradation experiments were repeated four times. The nanocatalysts exhibited significant and constant photocatalytic activity. The dye degradation efficiency does not alter through the process's four cycles, as shown in Figure 11. The results confirmed that Ru-ZnO@g-C₃N₄ nanomaterials have excellent stability throughout the degradation reaction.

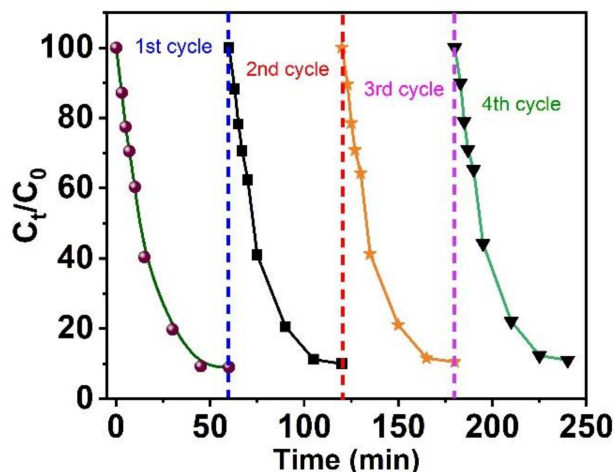


Figure 11. Photocatalytic cycling stability of Ru-ZnO@g-C₃N₄ photocatalyst nanoparticles.

3.6. Photocatalytic Mechanism

Experiments involving quenching were utilized to investigate the mechanism of the photocatalytic deterioration of MB dye on the fabricated nanocomposite. To capture e⁻, h⁺, ·OH, and ·O₂ in the solution, 50 mL of dye without scavenger, AgNO₃, EDTA, isopropanol (IPL), and ascorbic acid (ASC) were added to 50 mL of a solution containing 20 mg/L MB dye. In photocatalytic reactions, active molecules can be generated by a variety of mechanisms. The addition of EDTA and isopropanol hastened the breakdown of MB dye under UV illumination, whereas the addition of AgNO₃ and ASC had little effect; see Figure 12. The results revealed that ·O₂ and e⁻ contributed negligibly to the photocatalytic activity, but ·OH and h⁺ played a substantial role [36].

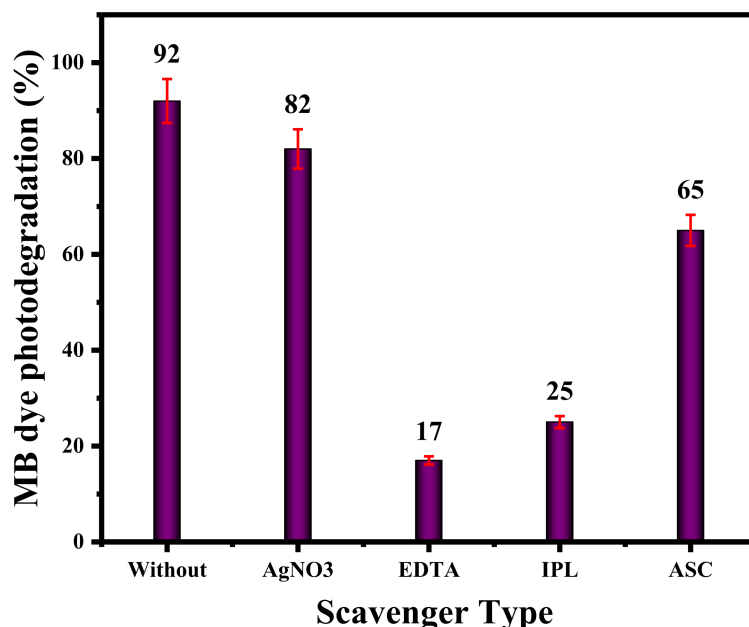
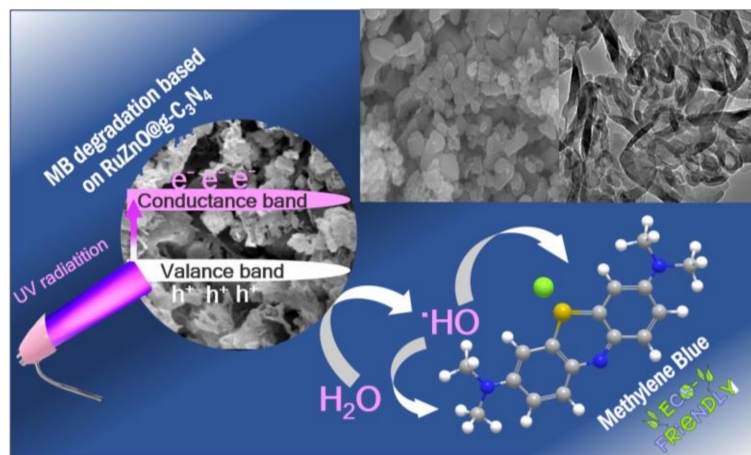


Figure 12. Quenching experiments of the proposed mechanism.

In principle, a photogenerated hole can react with water molecules to form hydroxyl radicals, which can subsequently react with MB molecules to decompose them into CO₂ and H₂O. Similarly, photogenerated holes can interact directly with MB dye molecules. The cationic dye MB degradation products under UV include CO₂, H₂O, and mineral acids, as shown in the schematic diagram (Scheme 1). Thus, this helps the conversion of various pollutants to environmental and eco-friendly species. The advanced oxidation method is

a process developed for converting toxic organic pollutants into eco-friendly molecules such as H_2O and CO_2 . Additionally, Ru-ZnO@g-C₃N₄ nanomaterials provide significant radicals that participate in the oxidation process to turn the organic pollutant molecules successfully into harmless molecules.



Scheme 1. Degradation mechanism of MB dye.

4. Conclusions

The research group attained the efficacious manufacture of a Ru-ZnO@g-C₃N₄ hetero-junction photocatalyst through the combination of g-C₃N₄ and Ru-ZnO nanostructures. The affection of Ru-ZnO nanostructures for the g-C₃N₄ was authenticated, where the XRD peak analysis exhibited the development of the Ru-ZnO along with characteristic g-C₃N₄ peaks. The morphological, EDX, and XPS data confirmed the nanocomposite's formation, showing improved optical properties. The photocatalytic competence of the Ru-ZnO@g-C₃N₄ was evaluated by MB degradation under ultraviolet light. The superior photocatalytic performance was attributed to the Z-scheme heterojunction formed by ZnO and g-C₃N₄ coupling that promoted efficient photo-excited charge-carrier separation. The photodegradation mechanism was consistent with the trapping experiments in which ·O₂ and e⁻ contributed negligibly to the photocatalytic activity, but ·OH and h⁺ played a substantial role. These new intuitions will help develop innovative strategies for future photocatalytic applications. Additionally, we are looking forward to using these nanomaterials in the removal processes for different types of toxic molecules.

Author Contributions: Conceptualization, S.M.S., M.A.B.A. and A.M.; methodology, A.M., S.M.S. and A.E.A.E.A.; formal analysis, S.M.S., M.A.B.A., A.E.A.E.A. and A.M.; investigation, S.M.S., M.A.B.A., A.M. and A.E.A.E.A.; resources, S.M.S., A.E.A.E.A. and A.M.; data curation, S.M.S. and A.M.; writing—original draft preparation, S.M.S., A.E.A.E.A., M.A.B.A. and A.M.; writing—review and editing, S.M.S. and A.M.; supervision, S.M.S., M.A.B.A. and A.M. All authors have read and agreed to the published version of the manuscript.

Funding: The authors extend their appreciation to the Deputyship for Research and Innovation, Ministry of Education, Saudi Arabia for funding this research work through the project number (QU-IF-4-3-2-29873). The authors also thank Qassim University for technical support.

Data Availability Statement: Not applicable.

Acknowledgments: The authors extend their appreciation to the Deputyship for Research and Innovation, Ministry of Education, Saudi Arabia for funding this research work through the project number (QU-IF-4-3-2-29873). The authors also thank Qassim University for technical support.

Conflicts of Interest: The authors declare no conflict of interest.

References

1. Vattikuti, S.P.; Reddy, P.A.K.; Shim, J.; Byon, C. Visible-light-driven photocatalytic activity of SnO₂–ZnO quantum dots anchored on g-C₃N₄ nanosheets for photocatalytic pollutant degradation and H₂ production. *ACS Omega* **2018**, *3*, 7587–7602. [[CrossRef](#)] [[PubMed](#)]
2. Taha, K.K.; Modwi, A.; Elamin, M.; Arasheed, R.; AL-Fahad, A.J.; Albutairi, I.; Alfaify, M.; Anojaidi, K.; Algethami, F.K.; Bagabas, A. Impact of Hibiscus extract on the structural and activity of sonochemically fabricated ZnO nanoparticles. *J. Photochem. Photobiol. A Chem.* **2020**, *390*, 112263. [[CrossRef](#)]
3. Kerrami, A.; Khezami, L.; Bououdina, M.; Mahtout, L.; Modwi, A.; Rabhi, S.; Bensouici, F.; Belkacemi, H. Efficient photodegradation of azucryl red by copper-doped TiO₂ nanoparticles—Experimental and modeling studies. *Environ. Sci. Pollut. Res.* **2021**, *28*, 57543–57556. [[CrossRef](#)] [[PubMed](#)]
4. Wang, W.W.; Zhu, Y.J.; Yang, L.X. ZnO–SnO₂ hollow spheres and hierarchical nanosheets: Hydrothermal preparation, formation mechanism, and photocatalytic properties. *Adv. Funct. Mater.* **2007**, *17*, 59–64. [[CrossRef](#)]
5. Liu, Z.; Wang, H.; Pan, G.; Niu, J.; Feng, P. Facile synthesis, structure and enhanced photocatalytic activity of novel BiOBr/Bi(C₂O₄) OH composite photocatalysts. *J. Colloid Interface Sci.* **2017**, *486*, 8–15. [[CrossRef](#)]
6. Li, Y.; Wang, H.; Xie, L.; Liang, Y.; Hong, G.; Dai, H. MoS₂ nanoparticles grown on graphene: An advanced catalyst for the hydrogen evolution reaction. *J. Am. Chem. Soc.* **2011**, *133*, 7296–7299. [[CrossRef](#)]
7. Modwi, A.; Ghanem, M.A.; Al-Mayouf, A.M.; Houas, A. Lowering energy band gap and enhancing photocatalytic properties of Cu/ZnO composite decorated by transition metals. *J. Mol. Struct.* **2018**, *1173*, 1–6. [[CrossRef](#)]
8. Modwi, A.; Mustafa, B.; Ismail, M.; Makawi, S.Z.; Hussein, T.I.; Abaker, Z.M.; Mujawah, A.; Al-Ayed, A.S. Physicochemical and photocatalytic performance of the synthesized RuO₂–ZnO photo-composite in the presence of pectinose solution. *Environ. Nanotechnol. Monit. Manag.* **2021**, *15*, 100403. [[CrossRef](#)]
9. Han, Q.; Zhao, F.; Hu, C.; Lv, L.; Zhang, Z.; Chen, N.; Qu, L. Facile production of ultrathin graphitic carbon nitride nanoplatelets for efficient visible-light water splitting. *Nano Res.* **2015**, *8*, 1718–1728. [[CrossRef](#)]
10. Kang, Y.; Yang, Y.; Yin, L.C.; Kang, X.; Wang, L.; Liu, G.; Cheng, H.M. Selective breaking of hydrogen bonds of layered carbon nitride for visible light photocatalysis. *Adv. Mater.* **2016**, *28*, 6471–6477. [[CrossRef](#)]
11. Zhang, C.; Liu, J.; Huang, X.; Chen, D.; Xu, S. Multistage polymerization design for g-C₃N₄ nanosheets with enhanced photocatalytic activity by modifying the polymerization process of melamine. *ACS Omega* **2019**, *4*, 17148–17159. [[CrossRef](#)]
12. Zhang, G.; Lan, Z.-A.; Lin, L.; Lin, S.; Wang, X. Overall water splitting by Pt/gC₃N₄ photocatalysts without using sacrificial agents. *Chem. Sci.* **2016**, *7*, 3062–3066. [[CrossRef](#)]
13. Alhaddad, M.; Mohamed, R.M.; Mahmoud, M.H. Promoting Visible Light Generation of Hydrogen Using a Sol–Gel-Prepared MnCo₂O₄@ g-CgC₃N₄ p–n Heterojunction Photocatalyst. *ACS Omega* **2021**, *6*, 8717–8725. [[CrossRef](#)]
14. Toghan, A.; Modwi, A. Boosting unprecedented indigo carmine dye photodegradation via mesoporous MgO@ g-CgC₃N₄ nanocomposite. *J. Photochem. Photobiol. A Chem.* **2021**, *419*, 113467. [[CrossRef](#)]
15. Toghan, A.; Abd El-Lateef, H.M.; Taha, K.K.; Modwi, A. Mesoporous TiO₂@ g-CgC₃N₄ composite: Construction, characterization, and boosting indigo carmine dye destruction. *Diam. Relat. Mater.* **2021**, *118*, 108491. [[CrossRef](#)]
16. Modwi, A.; Khezami, L.; Ghoniem, M.; Nguyen-Tri, P.; Baaloudj, O.; Guesmi, A.; Algethami, F.; Amer, M.; Assadi, A. Superior removal of dyes by mesoporous MgO/g-CgC₃N₄ fabricated through ultrasound method: Adsorption mechanism and process modeling. *Environ. Res.* **2022**, *205*, 112543. [[CrossRef](#)]
17. Jun, Y.S.; Hong, W.H.; Antonietti, M.; Thomas, A. Mesoporous, 2D hexagonal carbon nitride and titanium nitride/carbon composites. *Adv. Mater.* **2009**, *21*, 4270–4274. [[CrossRef](#)]
18. Xiao, J.; Xie, Y.; Li, C.; Kim, J.-H.; Tang, K.; Cao, H. Enhanced hole-dominated photocatalytic activity of doughnut-like porous g-C₃N₄ driven by down-shifted valance band maximum. *Catal. Today* **2018**, *307*, 147–153. [[CrossRef](#)]
19. Yang, P.; Zhao, J.; Qiao, W.; Li, L.; Zhu, Z. Ammonia-induced robust photocatalytic hydrogen evolution of graphitic carbon nitride. *Nanoscale* **2015**, *7*, 18887–18890. [[CrossRef](#)]
20. Mousavi, S.R.; Asghari, M.; Mahmoodi, N.M. Chitosan-wrapped multiwalled carbon nanotube as filler within PEBA thin film nanocomposite (TFN) membrane to improve dye removal. *Carbohydr. Polym.* **2020**, *237*, 116128. [[CrossRef](#)]
21. Cao, J.; Sun, S.; Li, X.; Yang, Z.; Xiong, W.; Wu, Y.; Jia, M.; Zhou, Y.; Zhou, C.; Zhang, Y. Efficient charge transfer in aluminum-cobalt layered double hydroxide derived from Co-ZIF for enhanced catalytic degradation of tetracycline through peroxymonosulfate activation. *Chem. Eng. J.* **2020**, *382*, 122802. [[CrossRef](#)]
22. Ghanbari, F.; Moradi, M. Application of peroxymonosulfate and its activation methods for degradation of environmental organic pollutants. *Chem. Eng. J.* **2017**, *310*, 41–62. [[CrossRef](#)]
23. Maiti, M.; Sarkar, M.; Xu, S.; Das, S.; Adak, D.; Maiti, S. Application of silica nanoparticles to develop faujasite nanocomposite for heavy metal and carcinogenic dye degradation. *Environ. Prog. Sustain. Energy* **2019**, *38*, S15–S23. [[CrossRef](#)]
24. Moheman, A.; Showkat, A.B.; Abu, T. *Aerogels for Waterborne Pollutants Purification. Advances in Aerogel Composites for Environmental Remediation*; Elsevier: Amsterdam, The Netherlands, 2021; pp. 109–124.
25. Xiang, W.; Wan, Y.; Zhang, X.; Tan, Z.; Xia, T.; Zheng, Y.; Gao, B. Adsorption of tetracycline hydrochloride onto ball-milled biochar: Governing factors and mechanisms. *Chemosphere* **2020**, *255*, 127057. [[CrossRef](#)]
26. Qiao, D.; Li, Z.; Duan, J.; He, X. Adsorption and photocatalytic degradation mechanism of magnetic graphene oxide/ZnO nanocomposites for tetracycline contaminants. *Chem. Eng. J.* **2020**, *400*, 125952. [[CrossRef](#)]

27. Wu, S.; Shen, L.; Lin, Y.; Yin, K.; Yang, C. Sulfite-based advanced oxidation and reduction processes for water treatment. *Chem. Eng. J.* **2021**, *414*, 128872. [[CrossRef](#)]
28. Li, Z.; Meng, X.; Zhang, Z. Fabrication of surface hydroxyl modified gC₃N₄ with enhanced photocatalytic oxidation activity. *Catal. Sci. Technol.* **2019**, *9*, 3979–3993. [[CrossRef](#)]
29. Elmorsi, T.M.; Elsayed, M.H.; Bakr, M.F. Enhancing the removal of methylene blue by modified ZnO nanoparticles: Kinetics and equilibrium studies. *Can. J. Chem.* **2017**, *95*, 590–600. [[CrossRef](#)]
30. Zhang, B.; Zhang, C.; He, H.; Yu, Y.; Wang, L.; Zhang, J. Electrochemical synthesis of catalytically active Ru/RuO₂ core-shell nanoparticles without stabilizer. *Chem. Mater.* **2010**, *22*, 4056–4061. [[CrossRef](#)]
31. Shen, C.; Chen, C.; Wen, T.; Zhao, Z.; Wang, X.; Xu, A. Superior adsorption capacity of g-C₃N₄ for heavy metal ions from aqueous solutions. *J. Colloid Interface Sci.* **2015**, *456*, 7–14. [[CrossRef](#)]
32. Mustafa, B.; Modwi, A.; Ismail, M.; Makawi, S.; Hussein, T.; Abaker, Z.; Khezami, L. Adsorption performance and Kinetics study of Pb (II) by RuO₂-ZnO nanocomposite: Construction and Recyclability. *Int. J. Environ. Sci. Technol.* **2022**, *19*, 327–340. [[CrossRef](#)]
33. Wang, X.; Wang, S.; Hu, W.; Cai, J.; Zhang, L.; Dong, L.; Zhao, L.; He, Y. Synthesis and photocatalytic activity of SiO₂/g-C₃N₄ composite photocatalyst. *Mater. Lett.* **2014**, *115*, 53–56. [[CrossRef](#)]
34. Modwi, A.; Abbo, M.; Hassan, E.; Houas, A. Effect of annealing on physicochemical and photocatalytic activity of Cu5% loading on ZnO synthesized by sol-gel method. *J. Mater. Sci. Mater. Electron.* **2016**, *27*, 12974–12984. [[CrossRef](#)]
35. Li, F.; Zhao, R.; Yang, B.; Wang, W.; Liu, Y.; Gao, J.; Gong, Y. Facial synthesis of dandelion-like g-C₃N₄/Ag with high performance of photocatalytic hydrogen production. *Int. J. Hydrogen Energy* **2019**, *44*, 30185–30195. [[CrossRef](#)]
36. Singh, J.; Arora, A.; Basu, S. Synthesis of coral like WO₃/g-C₃N₄ nanocomposites for the removal of hazardous dyes under visible light. *J. Alloys Compd.* **2019**, *808*, 151734. [[CrossRef](#)]
37. Saleh, S.M.; Albadri, A.E.A.E.; Aissa, M.A.B.; Modwi, A. Fabrication of Mesoporous V₂O₅@g-C₃N₄ Nanocomposite as Photocatalyst for Dye Degradation. *Crystals* **2022**, *12*, 1766. [[CrossRef](#)]
38. Lu, L.; Wang, G.; Zou, M.; Wang, J.; Li, J. Effects of calcining temperature on formation of hierarchical TiO₂/g-C₃N₄ hybrids as an effective Z-scheme heterojunction photocatalyst. *Appl. Surf. Sci.* **2018**, *441*, 1012–1023. [[CrossRef](#)]
39. Katsumata, H.; Tachi, Y.; Suzuki, T.; Kaneco, S. Z-scheme photocatalytic hydrogen production over WO₃/g-C₃N₄ composite photocatalysts. *RSC Adv.* **2014**, *4*, 21405–21409. [[CrossRef](#)]
40. Weingärtner, R.; Torres, J.G.; Erlenbach, O.; De La Puente, G.G.; De Zela, F.; Winnacker, A. Bandgap engineering of the amorphous wide bandgap semiconductor (SiC)_{1-x}(AlN)_x doped with terbium and its optical emission properties. *Mater. Sci. Eng. B* **2010**, *174*, 114–118. [[CrossRef](#)]
41. Lu, J.; Wang, Y.; Huang, J.; Cao, L.; Li, J.; Hai, G.; Bai, Z. One-step synthesis of g-C₃N₄ hierarchical porous structure nanosheets with dramatic ultraviolet light photocatalytic activity. *Mater. Sci. Eng. B* **2016**, *214*, 19–25. [[CrossRef](#)]
42. Mahmoodi, N.M.; Oveisi, M.; Bakhtiari, M.; Hayati, B.; Shekarchi, A.A.; Bagheri, A.; Rahimi, S. Environmentally friendly ultrasound-assisted synthesis of magnetic zeolitic imidazolate framework-Graphene oxide nanocomposites and pollutant removal from water. *J. Mol. Liq.* **2019**, *282*, 115–130. [[CrossRef](#)]
43. Mahmoodi, N.M.; Bashiri, M.; Moeen, S.J. Synthesis of nickel-zinc ferrite magnetic nanoparticle and dye degradation using photocatalytic ozonation. *Mater. Res. Bull.* **2012**, *47*, 4403–4408. [[CrossRef](#)]
44. Kumar, S.; Tonda, S.; Baruah, A.; Kumar, B.; Shanker, V. Synthesis of novel and stable gC₃N₄/N-doped SrTiO₃ hybrid nanocomposites with improved photocurrent and photocatalytic activity under visible light irradiation. *Dalton Trans.* **2014**, *43*, 16105–16114. [[CrossRef](#)]
45. Zhou, J.; Ji, X.; Zhou, X.; Guo, J.; Sun, J.; Liu, Y. Three-dimensional g-C₃N₄/MgO composites as a high-performance adsorbent for removal of Pb (II) from aqueous solution. *Sep. Sci. Technol.* **2019**, *54*, 2817–2829. [[CrossRef](#)]
46. Sun, L.; Zhao, X.; Jia, C.-J.; Zhou, Y.; Cheng, X.; Li, P.; Liu, L.; Fan, W. Enhanced visible-light photocatalytic activity of gC₃N₄-ZnWO₄ by fabricating a heterojunction: Investigation based on experimental and theoretical studies. *J. Mater. Chem.* **2012**, *22*, 23428–23438. [[CrossRef](#)]
47. Uddin, M.T.; Nicolas, Y.; Olivier, C.; Toupance, T.; Müller, M.M.; Kleebe, H.-J.; Rachut, K.; Ziegler, Jr.; Klein, A.; Jaegermann, W. Preparation of RuO₂/TiO₂ mesoporous heterostructures and rationalization of their enhanced photocatalytic properties by band alignment investigations. *J. Phys. Chem. C* **2013**, *117*, 22098–22110. [[CrossRef](#)]
48. Al-Gaashani, R.; Radiman, S.; Daud, A.; Tabet, N.; Al-Douri, Y. XPS and optical studies of different morphologies of ZnO nanostructures prepared by microwave methods. *Ceram. Int.* **2013**, *39*, 2283–2292. [[CrossRef](#)]
49. Zang, Y.-N.; Yang, S.-S.; Ding, J.; Zhao, S.-Y.; Chen, C.-X.; He, L.; Ren, N.-Q. A biochar-promoted V₂O₅/gC₃N₄Z-Scheme heterostructure for enhanced simulated solar light-driven photocatalytic activity. *RSC Adv.* **2021**, *11*, 15106–15117. [[CrossRef](#)]
50. Manríquez, M.E.; Noreña, L.E.; Wang, J.A.; Chen, L.; Salmones, J.; González-García, J.; Reza, C.; Tzompantzi, F.; Hernández Cortez, J.G.; Ye, L. One-pot synthesis of Ru-doped ZnO oxides for photodegradation of 4-chlorophenol. *Int. J. Photoenergy* **2018**, *2018*. [[CrossRef](#)]
51. Saleh, S.M. Metal oxide nanomaterials as photo-catalyst for dye degradation. *Res. Dev. Mater. Sci* **2019**, *9*, 1–8. [[CrossRef](#)]
52. Balcha, A.; Yadav, O.P.; Dey, T. Photocatalytic degradation of methylene blue dye by zinc oxide nanoparticles obtained from precipitation and sol-gel methods. *Environ. Sci. Pollut. Res.* **2016**, *23*, 25485–25493. [[CrossRef](#)]

53. Shanthi, M.; Kuzhalosai, V. Photocatalytic Degradation of An Azo Dye, Acid Red 27, in Aqueous Solution Using Nano ZnO. 2012. Available online: <http://nopr.niscares.in/bitstream/123456789/13656/1/IJCA%2051%283%29%20428-434.pdf> (accessed on 17 January 2023).
54. Zhang, L.; Cheng, H.; Zong, R.; Zhu, Y. Photocorrosion suppression of ZnO nanoparticles via hybridization with graphite-like carbon and enhanced photocatalytic activity. *J. Phys. Chem. C* **2009**, *113*, 2368–2374. [[CrossRef](#)]
55. Ahmad, M.; Ahmed, E.; Hong, Z.; Ahmed, W.; Elhissi, A.; Khalid, N. Photocatalytic, sonocatalytic and sonophotocatalytic degradation of Rhodamine B using ZnO/CNTs composites photocatalysts. *Ultrason. Sonochemistry* **2014**, *21*, 761–773. [[CrossRef](#)]
56. Katowah, D.F.; Saleh, S.M.; Alqarni, S.A.; Ali, R.; Mohammed, G.I.; Hussein, M.A. Network structure-based decorated CPA@CuO hybrid nanocomposite for methyl orange environmental remediation. *Sci. Rep.* **2021**, *11*, 1–21.
57. Saleh, S.M. ZnO nanospheres based simple hydrothermal route for photocatalytic degradation of azo dye. *Spectrochim. Acta Part A Mol. Biomol. Spectrosc.* **2019**, *211*, 141–147. [[CrossRef](#)]
58. Katowah, D.F.; Saleh, S.M.; Mohammed, G.I.; Alkayal, N.S.; Ali, R.; Hussein, M.A. Ultra-efficient hybrid material-based cross-linked PANI@ Cs-GO-OXS/CuO for the photocatalytic degradation of Rhodamine-B. *J. Phys. Chem. Solids* **2021**, *157*, 110208. [[CrossRef](#)]

Disclaimer/Publisher’s Note: The statements, opinions and data contained in all publications are solely those of the individual author(s) and contributor(s) and not of MDPI and/or the editor(s). MDPI and/or the editor(s) disclaim responsibility for any injury to people or property resulting from any ideas, methods, instructions or products referred to in the content.